PHYSICAL REVIEW A **104**, 033107 (2021)

Optimal control for suppressing wave-packet spreading with strong nonresonant laser pulses

Yukiyoshi Ohtsuki[*] and Tomotaro Namba
Department of Chemistry, Graduate School of Science, Tohoku University 6-3 Aramaki Aza-Aoba, Aoba-ku, Sendai 980-8578, Japan

Hiroyuki Katsuki
Graduate School of Science and Technology, Nara Institute of Science and Technology 8916-5 Takayama-cho, Ikoma, Nara 630-0192, Japan and Institute for Molecular Science, National Institutes of Natural Sciences Myodaiji, Okazaki 444-8585, Japan

Kenji Ohmori
Institute for Molecular Science, National Institutes of Natural Sciences Myodaiji, Okazaki 444-8585, Japan and The Graduate University for Advanced Studies (SOKENDAI) Shonan Village, Hayama, Kanagawa 240-0193, Japan

(Received 15 April 2021; accepted 26 August 2021; published 14 September 2021)

We use nonlinear optimal control simulation to systematically examine how to suppress wave-packet spreading with strong nonresonant near-infrared (NIR) laser pulses through a case study of a vibrational wave packet in the B state of I_2. As the degree of spreading of the vibrational wave packet is controllable by adjusting the pump pulse shape, the vibrational wave packet may be regarded as a prototype system to study spreading suppression by using nonresonant laser pulses. We quantitatively define spreading suppression in terms of the probability of finding the wave packet in the analytically defined, initially excited state at every vibrational period. From optimal control simulation and simulation by using model Gaussian pulse trains that mimic optimal pulses, we conclude that a simple periodic NIR pulse train *without* highly tuned temporal widths, amplitudes, or irradiation timings can almost perfectly stop the wave-packet spreading over a long control period, provided that the degree of spreading is not too large.

DOI: 10.1103/PhysRevA.104.033107

I. INTRODUCTION

An isolated quantum wave packet spreads with time even if it is bounded in a potential, except for a harmonic potential. The wave-packet spreading often referred to as dephasing is attributed to the anharmonicity of the potential that causes different time evolution of the relative phases of the eigenstates involved in the wave packet. Contrary to an open quantum system, in which the system coherence leaks to its environment due to the quantum entanglement between them [1,2], the isolated wave packet is free from the leak of coherence. Even so, controlling the relative phases to suppress the wave-packet spreading is not an easy task. Much effort has been devoted to realizing nondispersive wave packets in various systems such as electronic wave packets in Rydberg states [3–5], Bose-Einstein condensates [6,7], and so on [8].

Recently, we experimentally observed that a nonresonant near-infrared (NIR) laser pulse (hereinafter, NIR pulse) with a specific irradiation timing can selectively induce the phase shift of a vibrational wave packet in the B state of I_2 [9]. We also adopted a minimal model that consists of three states with an equally distributed initial condition and showed analytically that a NIR pulse train with a specified intensity at the right timing can stop the wave-packet spreading [9]. The use of the NIR pulse is advantageous as there is virtually no restriction on the choice of the central frequency [10,11]. In addition, we can freely adjust the spreading behavior of the vibrational wave packet by shaping the pump pulse. The relative phases of the eigenstates in the controlled wave-packet dynamics can be precisely measured by ultrafast molecular spectroscopy [12–14]. These features make the vibrational wave packet suitable to systematic studies of dephasing suppression control by using NIR pulses.

The purpose of the present study is to extend the dephasing suppression method to more general cases than those elaborated upon in our previous study [9,15]. For the sake of systematic study, we adopt the nonlinear optimal control simulation developed in our group [16,17] to design optimal NIR pulses to suppress the dephasing of various B state wave packets. The optimal-control approach [18–20] is useful because it provides a general and flexible way to design control pulses not only in molecular systems [21] but also in a wide range of systems such as spins in nitrogen-vacancy (NV) color centers in diamond [22,23], atom interferometry [24], Bose-Einstein condensates [25], and so on. It is also worth noting that, in addition to the present simulation method [16,17], there are several effective methods to solve optimal control problems [26–34]. The examples include the Krotov variant of monotonic convergent algorithms [29,30] and the first- and second-order gradient ascent pulse engineering (GRAPE) algorithms [31,32], some of which are provided by the software packages, e.g., SPINACH library [33].

In the present simulation, the wave packets are initially generated by pump pulses with systematically varied temporal widths. It is, however, not trivial to formulate the dephas-

---

[*] yukiyoshi.ohtsuki.d2@tohoku.ac.jp

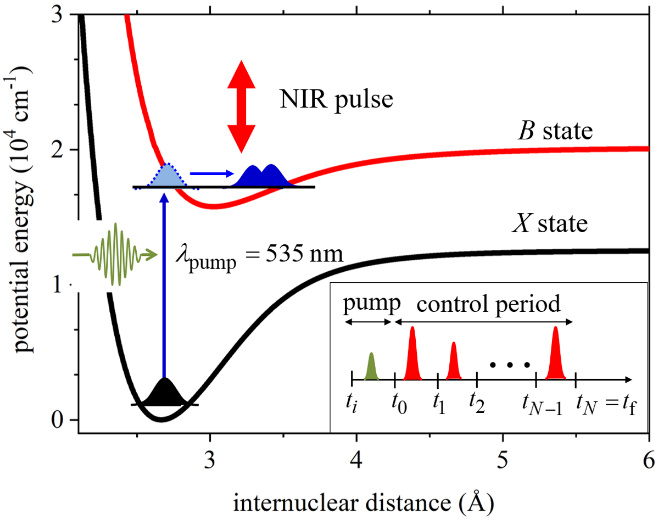

FIG. 1. Potential energy curves [35,36] and illustration of present scheme of dephasing-suppression control. Inset shows pulse sequence together with times that specify pump and control periods, $[t_{\rm i},\ t_0]$ and $[t_0,\ t_N = t_{\rm f}]$, respectively (see text).

ing suppression as an optimal control problem. For example, we have to quantitatively represent the degree of dephasing suppression that is suitable for our control objective, appropriately choose a final time, and so on. In Sec. II, we introduce the Hamiltonian and examine the role of the NIR pulse. In Sec. III, we outline the optimal control simulation together with numerical details (Appendix A). In Sec. IV, after defining the present target states, we show the results with a single target, those with multiple targets, and those derived by model Gaussian pulse trains that mimic the optimal NIR pulses. We summarize the present study in Sec. V.

II. NONRESONANT LASER PULSES AND WAVE-PACKET SPREADING

Figure 1 shows the two-electronic-state model that represents the X and B states of I_2 molecules. The molecules interact with the pump pulse, $E_{\rm pump}(t)$, which induces the resonant electronic transitions between the X and B states. They are assumed to interact with the nonresonant near-infrared laser pulse (NIR pulse) $E_{\rm NIR}(t)$ through the polarizability, i.e., the lowest-order induced-dipole moment within each electronic state. The dynamics is described by the Schrödinger equation:

$$i\hbar\frac{\partial}{\partial t}\begin{bmatrix}|\psi_B(t)\rangle\\|\psi_X(t)\rangle\end{bmatrix} = \begin{bmatrix}H_B(t) & -\mu_{BX}(r)E_{\rm pump}(t)\\ -\mu_{XB}(r)E_{\rm pump}(t) & H_X(t)\end{bmatrix} \times \begin{bmatrix}|\psi_B(t)\rangle\\|\psi_X(t)\rangle\end{bmatrix}, \quad (1)$$

where $|\psi_B(t)\rangle$ and $|\psi_X(t)\rangle$ are the vibrational wave packets in the B and X electronic states, respectively. If we assume that the molecule is in the lowest state at the initial time $t_{\rm i}$, the initial condition is given by $|\psi_B(t_{\rm i})\rangle = 0$ and $|\psi_X(t_{\rm i})\rangle = |0_X\rangle$ with $|0_X\rangle$ being the lowest vibrational state in the X state. The transition moment as a function of the internuclear distance, r, is given by $\mu_{BX}(r) = [\mu_{XB}(r)]^\dagger$. Because we assume the nonresonant NIR pulse, we take a cycle average over the central frequency of the NIR pulse in the polarizability interaction. We then have the B state Hamiltonian,

$$H_B(t) = H_B^0 - \frac{1}{4}\alpha_B(r)[\varepsilon(t)]^2, \quad (2)$$

where H_B^0, $\alpha_B(r)$, and $\varepsilon(t)$ are the field-free part of the Hamiltonian, a polarizability function, and an envelope function of the NIR pulse, respectively. The Hamiltonian H_B^0 is composed of the nuclear kinetic energy operator and the B state potential $V_B(r)$. Exchanging the suffix B for X in Eq. (2) gives the expression of the X state Hamiltonian $H_X(t)$. In the present study, we assume the pulse sequence in the inset of Fig. 1 so that there is no temporal overlap between the pump pulse and the NIR pulse. That is, we set $\varepsilon(t) = 0$ during $t \in [t_{\rm i},\ t_0]$, and $E_{\rm pump}(t) = 0$ during $t \in [t_0,\ t_{\rm f}]$ in Eqs. (1) and (2).

During the pump period specified with $[t_{\rm i},\ t_0]$, the vibrational wave packet in the B state, $|\psi_B(t)\rangle$, is generated by a pump pulse. The wave packet propagates on the B state potential, $V_B(r)$, and quickly spreads because the energy differences between the adjacent vibrational eigenstates in the wave packet depend on the vibrational quantum number due to the anharmonicity of $V_B(r)$. We then apply the NIR pulse to the B state wave packet to suppress its spreading, i.e., dephasing during the control period $[t_0,\ t_{\rm f}]$ motivated by what is described in the next paragraph.

When the NIR pulse is applied to the B state wave packet, the NIR pulse induces the Rayleigh and Raman scattering through the polarizability interaction. As all the eigenstates involved in the wave packet contribute to the scattering processes, the processes coherently interfere with each other depending on the relative phases among the eigenstates, i.e., the wave packet motion. In addition, the Stokes and anti-Stokes Raman scattering processes are shown to introduce extra phases into the eigenstates but with opposite phases [15]. The mixture of these quantum interferences characterizes the NIR-pulse-induced quantum interference, which leads to unique modification of the probability amplitude of each eigenstate, as we demonstrated in our previous study [37]. When we applied the NIR pulse to the wave packet in the B state of I_2, which was generated by a pump pulse, and measured the population of each eigenstate as a function of the time delay of the NIR pulse, we observed unusual quantum beats, i.e., "vibrational-state-resolved" quantum beats [37]. The quantum beats mean that the population of each eigenstate periodically changes as a function of time delay of the NIR pulse, suggesting that the NIR pulse delay can be used as a control knob of the populations. As a next step, it would be natural to expect that the phases of those eigenstates can also be controlled by the NIR pulse delay, and that phase control could lead to the suppression of the wave-packet spreading. The control for suppressing the wave-packet spreading requires that the NIR pulse should solely adjust the relative phases among the eigenstates, while avoiding the population redistribution to keep the original shape of the wave packet. We thus need to find the right irradiation timing, intensity, etc., in order for the NIR pulse to effectively cooperate with the wave-packet motion to suppress its spreading. Because we deal with various wave packets characterized by various degrees of dephasing, there are many factors to be considered to find such optimally designed NIR pulses, so that we employ the optimal control simulation [16–20], i.e., the full optimization approach, whose mathematical framework will be described in the next section.

III. OPTIMAL CONTROL SIMULATION

The optimal control simulation designs an external field to maximize a so-called objective functional that quantitatively measures the performance of our control. Mathematically, the objective functional is expressed as a function of the expectation value of a suitably chosen operator, which is often called a target operator, and specifies the control objective. The optimal control simulation is thus formulated as the maximization problem of the objective functional in the framework of calculus of variations, whose procedure will be described below in terms of the present case study for convenience.

The first step is to introduce a target operator W to specify the control objective. In the present study, we aim at periodically recovering the initially excited wave packet $|\chi\rangle$ so that the natural choice of the target operator would be $W = |\chi\rangle\langle\chi|$. This is because the expectation value of W has the maximum value when the wave packet exactly recovers the original shape, which mathematically specifies the control objective. We will examine how to determine $|\chi\rangle$ in Sec. IV.

The second step is to define the objective functional. As we typically adopt gradient-based iteration methods to obtain the external field that maximizes the objective functional, we may expect that the objective functional with the steeper gradient around the optimal solution would lead to better convergence behavior. In the present case, the steeper gradient could be realized by expressing the objective functional as a higher power of the expectation value of $W = |\chi\rangle\langle\chi|$. On the other hand, the complicated objective functional would increase computational cost. We thus need to find the balance between the fast convergence behavior and the computational cost. In the present study, we find that the objective functional in the form of the square of the expectation value shows reasonably good convergence behavior while introducing minimal extra computational cost. We thus adopt the following (unconstrained) objective functional expressed in terms of the density operator, $\rho(t) = |\psi(t)\rangle\langle\psi(t)|$,

$$\bar{J} = \langle\langle\rho(t_\mathrm{f})|W_\otimes|\rho(t_\mathrm{f})\rangle\rangle + \int_{t_0}^{t_\mathrm{f}} dt\langle\langle\rho(t)|Y_\otimes(t)|\rho(t)\rangle\rangle - 2\mathrm{Re}\int_{t_0}^{t_\mathrm{f}} dt\langle\langle\Xi(t)|\left[\frac{\partial}{\partial t} + \frac{i}{\hbar}L_B(t)\right]|\rho(t)\rangle\rangle, \tag{3}$$

in the Liouville-space notation [27,28,38]. In Eq. (3), we have used a normalized wave packet, $|\psi(t)\rangle = |\psi_B(t)\rangle/\sqrt{\langle\psi_B(t_0)\mid\psi_B(t_0)\rangle}$, instead of $|\psi_B(t)\rangle$ because we neglect the radiative relaxation and the electronic transitions induced by the NIR pulse. On the right-hand side of Eq. (3), the first term represents the square of the target expectation value at the final time, t_f. The Liouville-space operator $W_\otimes = \hat{W}\tilde{W}$ consists of the right-hand-acting operator $\hat{W}$ and the left-hand-acting operator $\tilde{W}$. In the second term, the intermediate target operator $Y_\otimes(t)$ [28] specifies the control objective during the control period. To be specific, this operator is introduced to suppress the dephasing over the control period, which will be defined below. The third term represents the constraint due to the equation of motion for $|\rho(t)\rangle\rangle$ by using the Lagrange multiplier density, $|\Xi(t)\rangle\rangle$. The Liouvillian $L_B(t)$ corresponds to the commutator $[H_B(t), \cdots]$.

Next, we consider how to specify the intermediate target operator $Y_\otimes(t)$ by using the present target operator $W = |\chi\rangle\langle\chi|$. Because the B state wave packet periodically oscillates with time while collapsing, we require that it recovers its "original" shape $|\chi\rangle$ at specified intermediate control times $\{t_n : n = 1,\ 2, \ldots,\ N-1\}$. We will treat $\{t_n\}$ in a general framework in this section although we could expect that $\{t_n\}$ should be close to the integral multiples of the vibrational period. We will examine how to choose $\{t_n\}$ in Sec. IV. The requirement leads to the intermediate target operator

$$Y_\otimes(t) = W_\otimes\sum_{n=1}^{N-1}\delta(t - t_n). \tag{4}$$

Because of Eq. (4), Eq. (3) is reduced to the sum of the functionals,

$$\bar{J} = \sum_{n=1}^{N}\left\{\langle\langle\rho(t_n)|W_\otimes|\rho(t_n)\rangle\rangle - 2\mathrm{Re}\int_{t_{n-1}}^{t_n} dt\langle\langle\Xi(t)|\left[\frac{\partial}{\partial t} + \frac{i}{\hbar}L_B(t)\right]|\rho(t)\rangle\rangle\right\} = \sum_{n=1}^{N}\bar{J}_n, \tag{5}$$

with $t_N = t_\mathrm{f}$. In the present study, we approximately regard Eq. (5) as the sum of independent objective functionals, $\{\bar{J}_n\ (n = 1, 2, \ldots, N)\}$.

The third step is to derive the coupled pulse-design equations. By applying the calculus of variations to each functional $\bar{J}_n$, we obtain the maximal condition that is expressed as an implicit function of the optimal envelope $\varepsilon(t)$,

$$\mathrm{Im}\langle\langle\Xi(t)|A_B(r)|\rho(t)\rangle\rangle\varepsilon(t) = 0, \tag{6}$$

where $A_B(r) \leftrightarrow [\alpha_B(r),\ \cdots]$ and the initial condition is given by $|\rho(t_{n-1})\rangle\rangle$. As we restrict ourselves to a pure state and assume the target operator $W = |\chi\rangle\langle\chi|$, the Lagrange multiplier density is expressed as $\Xi(t) = |\xi(t)\rangle\langle\xi(t)|$, where the wave function $|\xi(t)\rangle$, obeys the equation of motion,

$$i\hbar\frac{\partial}{\partial t}|\xi(t)\rangle = \left\{H_B^0 - \frac{1}{4}\alpha_B(r)[\varepsilon(t)]^2\right\}^\dagger|\xi(t)\rangle. \tag{7}$$

The final condition is given by $|\xi(t_n)\rangle = |\chi\rangle\langle\chi|\psi(t_n)\rangle$. Then, we express Eq. (6) in terms of $|\psi(t)\rangle$ and $|\xi(t)\rangle$, to obtain the maximal condition in the wave-function form:

$$\mathrm{Im}\langle\psi(t)|\xi(t)\rangle\langle\xi(t)|\alpha_B(r)|\psi(t)\rangle\varepsilon(t) = 0. \tag{8}$$

We solve the pulse-design equations iteratively by using the monotonically convergent algorithm developed in our previous study [16,17] to deal with the induced-dipole interaction

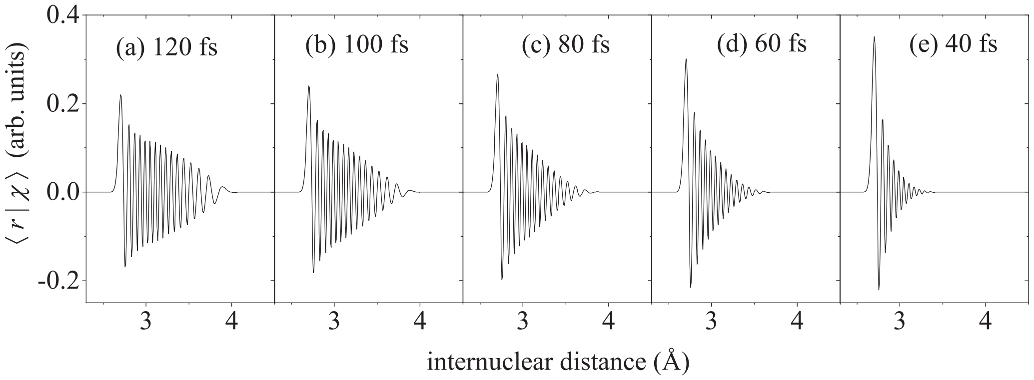

FIG. 2. Initially excited wave packets $|\chi\rangle$, [Eq. (10)] generated by Gaussian pump pulses with temporal widths of (a) 120, (b) 100, (c) 80, (d) 60, and (e) 40 fs.

[16,17,39–41]. The details of the present numerical solution are summarized in Appendix A.

IV. OPTIMAL CONTROL TO SUPPRESS WAVE-PACKET SPREADING

A. Target state preparation

We apply the general procedure described in Sec. III to the design of the optimal NIR pulses for suppressing wave-packet spreading. For this purpose, we need to explicitly define the target state, i.e., the initially excited state $|\chi\rangle$. If we assume that the pump pulse is sufficiently weak to be approximately treated by the lowest-order perturbation, then the first-order solution after the pump pulse is

$$\left|\psi_B^{1\text{st}}(t)\right\rangle = \frac{i}{\hbar}\int_{-\infty}^{\infty} dt_1 e^{-i(t-t_1)H_B^0/\hbar}\mu_{BX}(r)E_{\text{pump}}(t_1) \times e^{-i(t_1-t_i)H_X^0/\hbar}|0_X\rangle. \tag{9}$$

Because of $|\psi_B^{1\text{st}}(t)\rangle \propto e^{-iH_B^0 t/\hbar}|\chi\rangle$, it would be natural to define

$$|\chi\rangle = N_\chi \tilde{E}_{\text{pump}}\big(H_B^0/\hbar - \omega_{X0}\big)\mu_{BX}(r)|0_X\rangle \tag{10}$$

with a normalization constant N_χ [42]. The Fourier transform of the pump pulse is given by

$$\tilde{E}_{\text{pump}}\big(H_B^0/\hbar - \omega_{X0}\big) = \int_{-\infty}^{\infty} dt_1 e^{i(H_B^0/\hbar-\omega_{X0})t_1}E_{\text{pump}}(t_1), \tag{11}$$

where $\hbar\omega_{X0}$ is an energy eigenvalue of $|0_X\rangle$ defined by the eigenvalue equation, $H_X^0|0_X\rangle = \hbar\omega_{X0}|0_X\rangle$.

To more clearly illustrate the present target state $|\chi\rangle$ in Eq. (10), we show some of the examples that are used in the numerical applications in Sec. IV. We adopt the same molecular parameters as those used in our previous study [15,35,36,43–45]. We consider Gaussian pump pulses with temporal peaks at $t = 0$ fs and temporal widths [full width at half maximum (FWHM)] in the range of $\Delta\tau_{\text{pump}} \in [40\text{ fs}, 120\text{ fs}]$ so that we choose $t_{\text{i}} = -300$ fs and $t_0 = 300$ fs (Fig. 1). The central wavelength and the peak amplitude of the pump pulse are set to 535 nm and 3×10^6 V/m, respectively. We introduce the rotating-wave approximation and the so-called field interaction representation [46], which remove the rapidly oscillating components associated with the excitation by the pump pulse. The temporal grid size is set to 0.1 fs. The time evolution of the wave packets is solved by a standard method, i.e., the combination of a split-operator method and fast Fourier transform (FFT), in which the spatial range [2.1 Å, 6.0 Å] is equally divided into 512 grid points.

Figure 2 shows some examples of $|\chi\rangle$ generated by the Gaussian pump pulses with several temporal widths. As expected, we see that the initial wave packets approach the so-called Franck-Condon wave packets as the temporal width of the pump pulses decreases. Using $|\chi\rangle$ in Fig. 2, we calculate $|\langle\chi|\psi(t)\rangle|^2$ in Fig. 3. The time evolution of $|\langle\chi|\psi(t)\rangle|^2$ in Fig. 3(a) slowly collapses, which can be classified into a weak dephasing case, while that in Fig. 3(c) corresponds to an intermediate dephasing case. In Fig. 3(e), the first maximal value is already reduced to ca. 0.75, which means that the 40-fs Gaussian pump pulse corresponds to an extremely strong dephasing case. The considerably different collapse patterns are realized by adjusting the pump pulse width, which makes the present system suitable for systematically examining dephasing suppression.

B. Results and discussion

Here we show the results of optimal control simulation for suppressing the wave-packet spreading. For convenience, we introduce a dimensionless envelope function $f(t)$, defined by $\alpha_B(r)[\varepsilon(t)]^2 = V_\alpha(r)[f(t)]^2$. Here, $V_\alpha(r)$ is the magnitude of the polarizability interaction taken from Ref. [15], and has a value of $V_\alpha(r_{\text{e}}) = 1.3 \times 10^{-3}$ a.u. at the equilibrium nuclear distance in the B state, r_{e}. In Secs. IV B 1 and IV B 2, we consider the optimal control simulation with a single target [$N = 1$ in Eq. (5)] and that with multiple targets, respectively. In Sec. IV B 3, we discuss the dephasing suppression control by using the model Gaussian NIR pulses that mimic the fully optimized NIR pulses.

1. Optimal control simulation with a single target (N = 1) in a short control time case

We consider the simplest case of a single target with a "short" control time, $t_{\text{f}} = 2850$ fs, which corresponds to approximately six vibrational periods. The target value $|\langle\chi \mid \psi(t_{\text{f}})\rangle|^2$ is affected not only by the dephasing but also by the periodic motion of the wave packet. Here, we choose

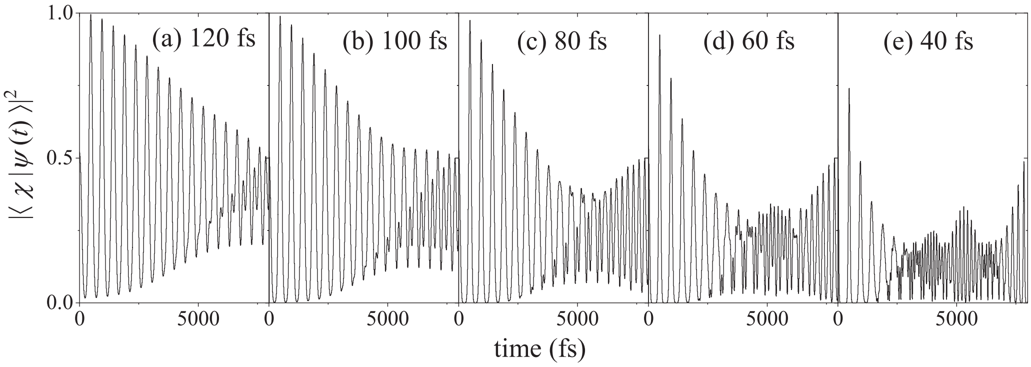

FIG. 3. Time evolution of $|\langle\chi|\psi(t)\rangle|^2$ when the B state wave packets are generated by Gaussian pump pulses with the temporal peak position $t = 0$. Temporal widths (FWHM) of the Gaussian pulses are set to (a) 120, (b) 100, (c) 80, (d) 60, and (e) 40 fs.

$t_f = 2850$ fs to reduce the latter effects. Note that we have numerically checked that $|\langle\chi \mid \psi(t_f)\rangle|^2$ is not extremely sensitive to the choice of t_f in preliminary simulations (not shown here). Assuming an 80-fs Gaussian pump pulse, we iteratively solve the pulse-design equations until $|\langle\chi \mid \psi(t_f)\rangle|^2$ reaches the value of 0.99.

The results are shown in Fig. 4, the features of which can be summarized as follows. The optimal envelope, i.e., the optimal pulse in Fig. 4(a), periodically appears with almost the same shape. We see from Figs. 4(a) and 4(b) that the temporal peak positions of the optimal pulse nearly coincide with those of $|\langle\chi|\psi(t)\rangle|^2$. The optimal pulse starts controlling the wave packet way before the dephasing of the wave packet becomes pronounced. Each peak intensity in Fig. 4(a) is almost the same as that used in our previous study to reproduce the experimentally observed NIR-induced effects on the quantum beats [9]. In spite of the high intensity, we see from Fig. 4(c) that the population of each vibrational eigenstate does not change so much. This feature is favorable because the population redistribution must change the shape of the wave packet, leading to the decrease in value of $|\langle\chi|\psi(t_f)\rangle|^2$. From these features, we suggest that there exist irradiation timings for the NIR pulse to adjust the relative phases among the vibrational eigenstates while minimizing the population transitions, which effectively suppresses the dephasing. As shown in Appendix B, this control mechanism could be explained by the interference between the original wave packet and the NIR-induced component. For reference, we show the results of more rigorous control that almost perfectly suppresses the dephasing in Appendix C.

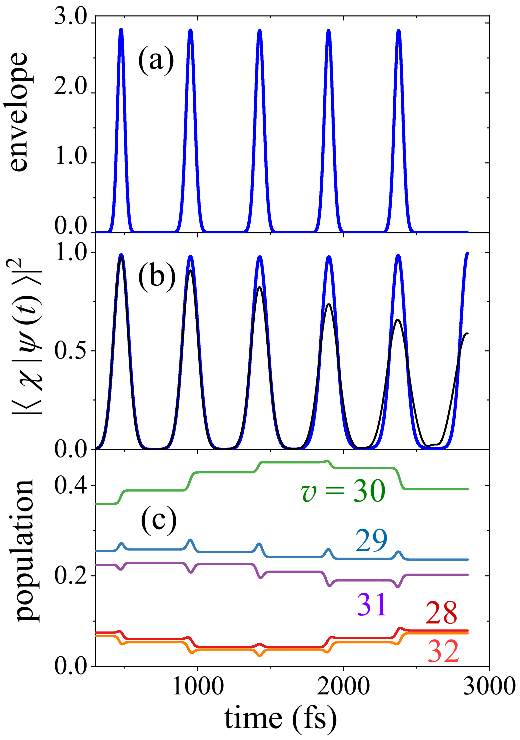

FIG. 4. Results of optimal control simulation are plotted as a function of time when a single target with a fixed control time $t_f = 2850$ fs is assumed. (a) Optimal envelope function $f(t)$, (b) $|\langle\chi|\psi(t)\rangle|^2$ with (blue line) and without (black line) the optimal pulse, and (c) time evolution of populations of five major vibrational eigenstates in $|\psi(t)\rangle$.

Next, we systematically change the temporal widths of the pump pulses, i.e., the degrees of dephasing as shown in Fig. 3, and design the optimal pulses that achieve $|\langle\chi|\psi(t_f)\rangle|^2 = 0.99$ at $t_f = 2850$ fs. The results are summarized in Fig. 5 (optimal envelope functions) and Fig. 6 (time evolution of $|\langle\chi|\psi(t)\rangle|^2$). We see from Figs. 5 and 6 that when $\Delta\tau_{\text{pump}} \geqslant 60$ fs, the optimal pulses have simple periodic structures and the wave packets tend to keep localized structures over the control period. On the other hand, the optimal pulse in the case of $\Delta\tau_{\text{pump}} = 40$ fs has a highly shaped structure. We thus conclude that a simple periodic NIR pulse can effectively suppress the dephasing, provided that the wave packet is not severely deformed by the anharmonicity within one vibrational period. It is also worth noting that the discussion based on the controlled dephasing in Figs. 5 and 6 confirms the advantages of using the vibrational wave packet to study the dephasing suppression.

2. Optimal control simulation with multiple targets ($N = 12$) in a long control time case

We consider the optimal control simulation with a long control time of around 5700 fs. Here, we focus on two pump

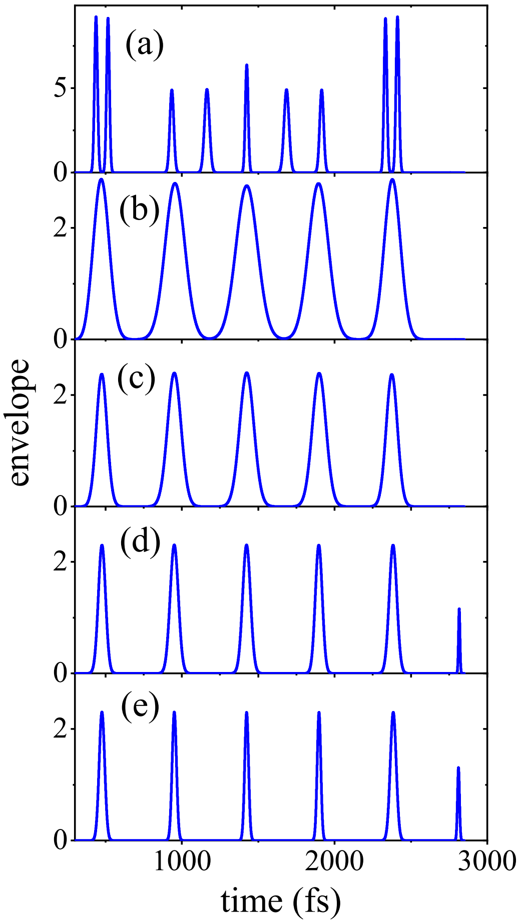

FIG. 5. Optimal envelope functions $f(t)$ when the temporal widths of the pump pulses are set to (a) 40, (b) 60, (c) 80 [same as that in Fig. 4(a)], (d) 100, and (e) 120 fs. Here, we assume a single target ($N = 1$) with a fixed control time $t_f = 2850$ fs.

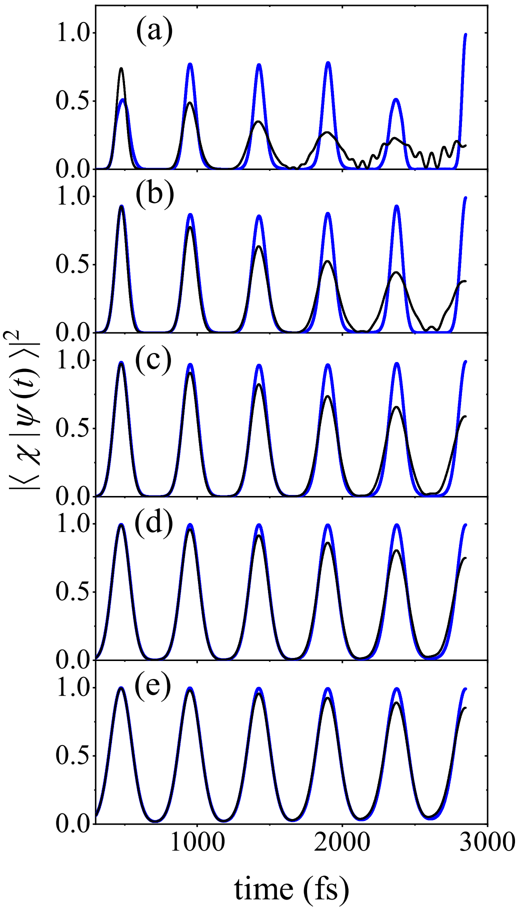

FIG. 6. Time evolution of $|\langle\chi|\psi(t)\rangle|^2$ under the control of the optimal pulses in Fig. 5, i.e., when the temporal widths of the pump pulses are set to (a) 40, (b) 60, (c) 80 [same as that in Fig. 4(b)], (d) 100, and (e) 120 fs. For reference, time evolution of $|\langle\chi|\psi(t)\rangle|^2$ in the absence of the optimal pulses is shown by black solid lines.

pulses with the temporal widths of 80 and 60 fs. In these cases, the wave packet considerably collapses around 5700 fs due to the anharmonicity in the absence of a NIR pulse (Fig. 3). We assume the intermediate and final control times at $t_n = nT_{\text{ho}}$ ($n = 1, 2, \ldots, N = 12$) as the initial guesses with a vibrational period T_{ho}. At every iteration step, we search the local maximum values of $|\langle\chi|\psi(t_n)\rangle|^2$ in the ranges of $[t_n - 40\text{ fs}, t_n + 40\text{ fs}]$ ($n = 1, 2, \ldots, 12$) and redefine the new control times, $\{t_n\}$. The iteration continues until the averaged maximum value $(1/12)\sum_n |\langle\chi|\psi(t_n)\rangle|^2$ becomes greater than 0.99 and 0.95 for the 80- and 60-fs pump pulses, respectively. The difference in convergence criteria originates from the different degrees of difficulty of the suppression control. Note that in both cases, the newly defined control times after the convergence are close to the initial guess times, $\{t_n = nT_{\text{ho}}\}$.

The results in the cases of the 80- and 60-fs pump pulses are shown in Figs. 7 and 8, respectively. We see that the results in Fig. 7 are similar to those in Fig. 4 in the sense that the optimal envelope, i.e., the optimal pulse, appears periodically with an almost regular time interval to almost completely suppress the dephasing [Fig. 7(b)]. On the other hand, some components of the optimal envelope in Fig. 8(a) have double-peak structures that are due to the difficulty in suppressing the dephasing [Fig. 8(b)]. The difference between the temporal structures of the optimal envelopes in Figs. 7(a) and 8(a) also leads to the different time-dependent behaviors of the populations in Figs. 7(c) and 8(c). Although there are some differences, the results in Figs. 7 and 8 would lead to the same conclusion as that derived in the previous subsection. That is, a NIR pulse with a simple periodic structure can suppress the dephasing with high probability, provided that the degree of dephasing is not too large during one vibrational period. To confirm this conclusion, we calculate $|\langle\chi|\psi(t)\rangle|^2$ by using a model pulse train in the next subsection.

3. Long control time with a Gaussian pulse train

The model pulse train considered here is composed of identical Gaussian pulses. For the sake of comparison, we assume almost the same final time as those used in Figs. 7 and 8 while fixing the temporal peak of each Gaussian control pulse at $t_n = nT_{\text{ho}}$ ($n = 1, 2, \ldots, 11$). We consider the three pump pulses with the temporal widths of 80, 60, and 40 fs. We calculate $|\langle\chi|\psi(t)\rangle|^2$ until ~5700 fs corresponding to the 12 vibrational periods ($t_{12} = t_f$). We thus search the 12

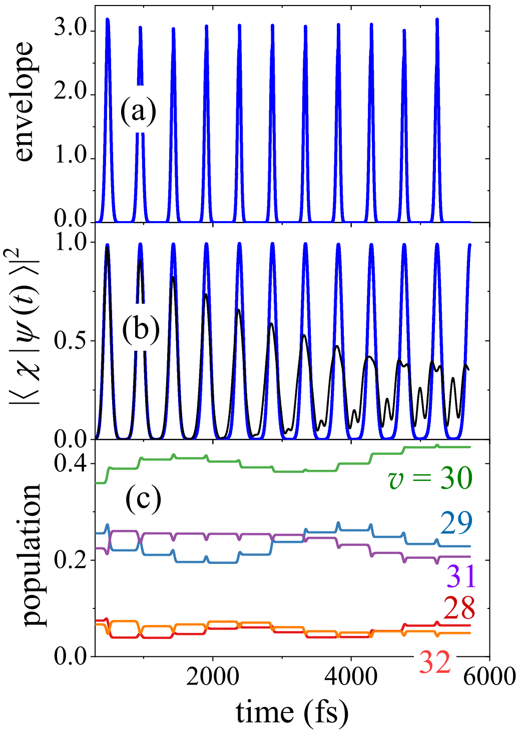

FIG. 7. Results of optimal control simulation when the temporal width (FWHM) of the pump pulse is set to 80 fs. Multiple targets ($N = 12$) with control time $t_{\mathrm{f}} \sim 5700$ fs are assumed. (a) Optimal envelope function $f(t)$, (b) $|\langle\chi|\psi(t)\rangle|^2$ with (blue line) and without (black line) the optimal pulse, and (c) time evolution of populations of five major vibrational eigenstates in $|\psi(t)\rangle$.

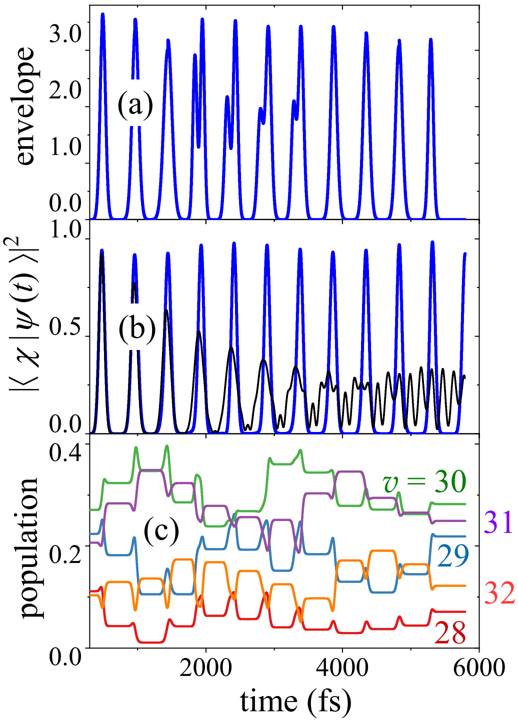

FIG. 8. Results of optimal control simulation when the temporal width (FWHM) of the pump pulse is set to 60 fs. Multiple targets ($N = 12$) with control time $t_{\mathrm{f}} \sim 5700$ fs are assumed. (a) Optimal envelope function $f(t)$, (b) $|\langle\chi|\psi(t)\rangle|^2$ with (blue line) and without (black line) the optimal pulse, and (c) time evolution of populations of five major vibrational eigenstates in $|\psi(t)\rangle$.

local maximum values around each "vibrational period" in the range of $[t_n - 50$ fs, $t_n + 50$ fs$]$ $(n = 1, 2, \ldots, N = 12)$. From each set of the 12 local maximum values, we calculate the averaged maximum value. In Fig. 9, we plot the averaged maximum values as a function of the dimensionless amplitude and the temporal width (FWHM) of $f(t)$ (a Gaussian envelope in this subsection). We see from Fig. 9(a) that the averaged maximum values greater than 0.98 are distributed in the wide range of the parameter space although the pulse fluence is slightly larger than that of the optimal pulse in Fig. 7(a). In Fig. 9(b), reasonably large, averaged maximum values appear in some regions, which, however, correspond to the large fluence. On the other hand, we cannot see such large averaged maximum values in Fig. 9(c); i.e., the values are always smaller than 0.75. Here, we emphasize that in most situations, we are interested in dealing with mildly large dephasing such as that in the case of the 80-fs pump pulse; that is, the examples in Figs. 9(b) and 9(c) do not mean the lack of usefulness of the present suppression control because the dephasing induced by the 60- and 40-fs pump pulses is extremely large, as shown in Fig. 3. In the following, we thus focus on the case of the 80-fs pump pulse.

In Fig. 10(a), we show the same results as those in Fig. 9(a) but assuming a longer final time, ~8000 fs. This final time corresponds to approximately 17 vibrational periods, meaning that the pulse train is composed of 16 Gaussian control pulses. Because the results in Fig. 10(a) are almost the same as those in Fig. 9(a), we can say that the simple pulse train suppresses the dephasing for a long period. In addition, as the averaged maximum values, $(1/12)\sum_n |\langle\chi \mid \psi(t_n)\rangle|^2$, greater than 0.98 are widely distributed [Fig. 10(a)], we do not need to highly tune the control pulse with respect to the temporal width or the amplitude of each Gaussian pulse. [We have virtually the same results as those in Fig. 10(a) even if we adopt an even longer final time, ~10 000 fs (not shown here).] So far, we have assumed a fixed irradiation timing at every "vibrational period," T_{ho}. We next relax this restriction.

In Figs. 10(b) and 10(c), the averaged maximum values $(1/12)\sum_n |\langle\chi|\psi(t_n)\rangle|^2$, as a function of the dimensionless amplitude, are shown when the temporal widths of the Gaussian control pulses in the pulse train are set to 70 and 50 fs, respectively. That is, we show the cuts of Fig. 10(a) along the temporal width of each Gaussian pulse, (b) 70 fs and (c) 50 fs, by using the black solid lines. Then, each temporal peak position of the Gaussian control pulse is randomly distributed in the ranges of $[t_n - 10$ fs, $t_n + 10$ fs$]$ $(n = 1, 2, \ldots, 16)$ by using random numbers. We prepare 20 sets of the 16 random numbers and calculate the averaged maximum values for each set in the same manner as we did in Fig. 9. We further take the average of the 20 sets of these averaged maximum values to obtain the values plotted by the blue solid lines in Figs. 10(b) and 10(c). Here, we use the notation $\langle\cdots\rangle$ in the titles of the vertical axes to emphasize the statistical average. We do the same calculations assuming the wider fluctuation range of $[t_n - 20$ fs, $t_n + 20$ fs$]$, and show the results by the purple solid lines in Figs. 10(b) and 10(c). These results suggest

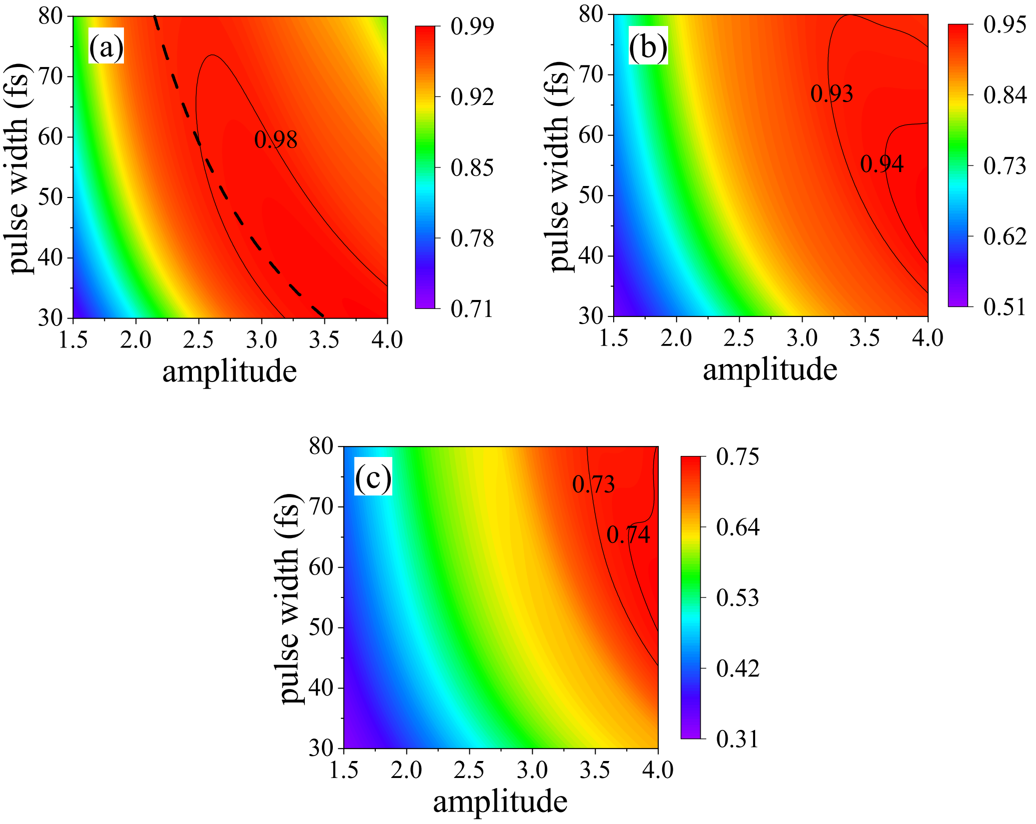

FIG. 9. Contour plots of averaged maximum values as a function of the dimensionless amplitude and the temporal width of each Gaussian pulse in the pulse train. The final time is set to ~5700 fs. The temporal widths of the pump pulses are set to (a) 80, (b) 60, and (c) 40 fs. In (a), the parameters that give the same pulse fluence as that of the optimal pulse in Fig. 7(a) are specified by the dashed line. Note that we adopt different color scales to clearly show the distribution patterns. The pulse train is composed of 11 Gaussian pulses that periodically appear at fixed timings, $t_n = nT_{\mathrm{ho}}$ $(n = 1,\ 2, \ldots,\ 11)$. We thus search the 12 local maximum values to calculate the averaged maximum values for each set of parameters. See text for details.

that we do not need to apply the Gaussian control pulses at rigorously predetermined timings; that is, if we adjust the irradiation timing of each pulse with ca. ±10 fs accuracy, the pulse train effectively suppresses the dephasing for a long control period with high probability.

V. SUMMARY

By using the nonlinear optimal control simulation, we have discussed a dephasing suppression method by using mildly intense NIR pulses through a case study of vibrational wave packets in the B state of I_2. As the wave packet is initially prepared by a pump pulse, the degree of dephasing of the wave packet due to the anharmonicity can be adjusted by the pump pulse. Thus, we may regard the vibrational wave packet as a prototype system to study the dephasing suppression. In the present study, we define the dephasing suppression such that the wave packet recovers the shape of the initially excited wave packet at every vibrational period. The dephasing suppression control is quantitatively evaluated by the square of the absolute value of the overlap between the wave packet and the analytically defined, initially excited state. Based on the present simulation, we have proposed a control method for suppressing the wave-packet spreading. That is, we have shown that a NIR pulse train composed of periodic pulses at every vibrational period can suppress the dephasing with high probability for the wave packets characterized by various degrees of dephasing, provided that the wave packet is not severely deformed within one vibrational period. It should be emphasized that the present suppression control does not require highly tuned pulse widths, amplitudes, or irradiation timings. Because of the robustness, we expect that the present dephasing suppression control would be a powerful tool to suppress the wave-packet spreading in a wide range of anharmonic systems.

ACKNOWLEDGMENTS

One of the authors (Y.O.) acknowledges support from JSPS KAKENHI Grant No. JP20K05414 and partly from the Joint Usage/Research Program on Zero-Emission Energy Research, Institute of Advanced Energy, Kyoto University (Grant No. ZE2021B-14). This work was supported by MEXT Quantum Leap Flagship Program (MEXT Q-LEAP) Grant No. JPMXS0118069021 and JSPS KAKENHI Grant No. JP16H06289 (Specially Promoted Research).

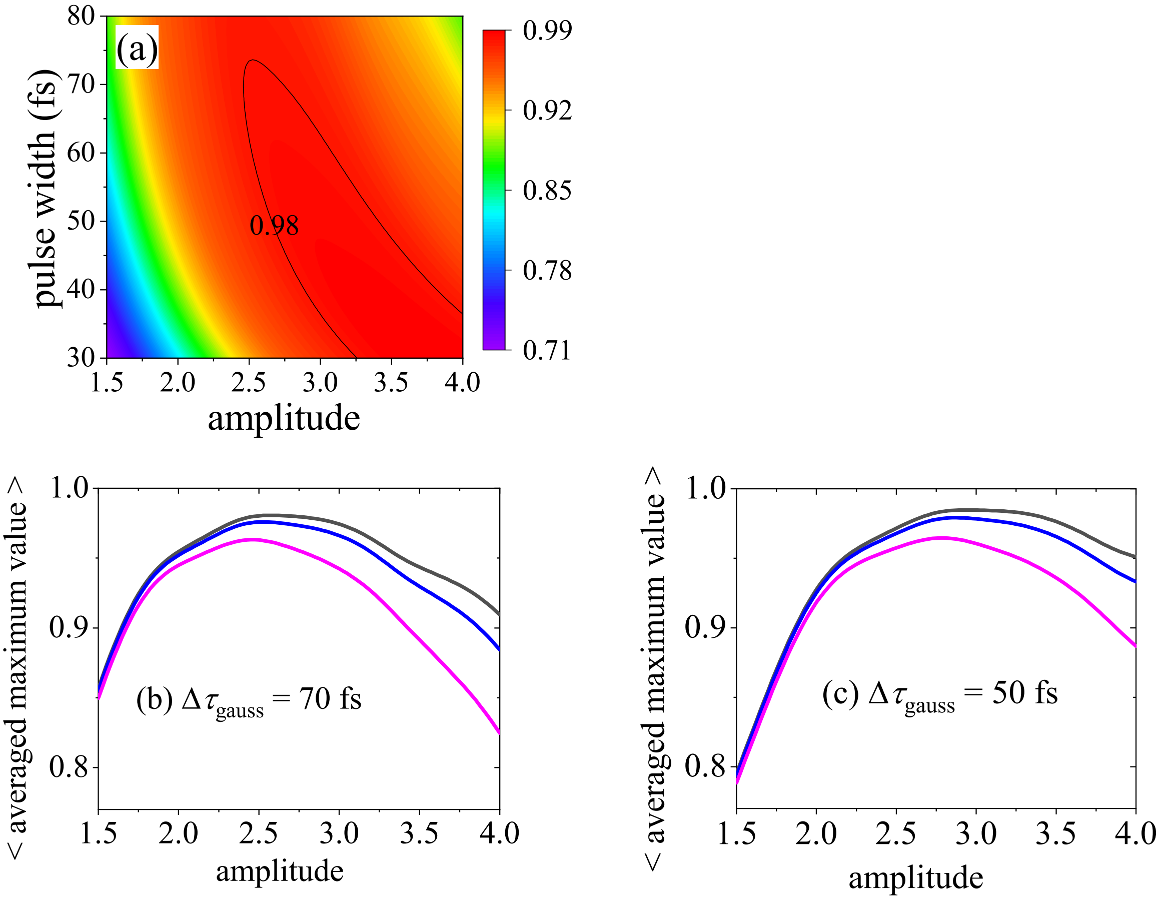

FIG. 10. (a) Contour plot of averaged maximum values as a function of the dimensionless amplitude and the temporal width of each Gaussian pulse in the pulse train. The final time is set to ~8000 fs, corresponding to a model pulse train composed of 16 Gaussian pulses. The temporal width of the pump pulses is set to 80 fs. The cuts along the temporal width of each Gaussian pulse, (b) 70 and (c) 50 fs, are shown by the black lines. In (b), (c), the blue and purple lines show the averaged maximum values that are calculated by assuming fluctuated irradiation timings, within the ranges of $[t_n - 10\ \mathrm{fs},\ t_n + 10\ \mathrm{fs}]$ and $[t_n - 20\ \mathrm{fs},\ t_n + 20\ \mathrm{fs}]$ $(n = 1,\ 2, \ldots,\ 16)$, respectively. See text for details.

APPENDIX A: MONOTONICALLY CONVERGENT ALGORITHM AND NUMERICAL DETAILS

We consider the coupled pulse-design equations derived from $\bar{J}_n$ and examine how to solve them using the monotonically convergent algorithm developed in our study. According to our previous study [16,17], the square of the envelope $[\varepsilon(t)]^2$ is expressed as the product of two artificial components such that $\varepsilon_1(t)\varepsilon_2(t)$. The pulse-design equations during $[t_{n-1},\ t_n]$ $(n = 1,\ 2,\ \ldots,\ N)$ at the kth step are summarized as follows:

$$i\hbar\frac{\partial}{\partial t}\big|\xi^{(k)}(t)\big\rangle = \left\{H_B^0 - \frac{1}{4}\alpha_B(r)\varepsilon_1^{(k)}(t)\varepsilon_2^{(k-1)}(t)\right\}^{\dagger}\big|\xi^{(k)}(t)\big\rangle, \tag{A1}$$

with the final condition, $|\xi^{(k)}(t_n)\rangle = |\chi\rangle\langle\chi|\psi^{(k)}(t_n)\rangle$, and

$$i\hbar\frac{\partial}{\partial t}\big|\psi^{(k)}(t)\big\rangle = \left\{H_B^0 - \frac{1}{4}\alpha_B(r)\varepsilon_1^{(k)}(t)\varepsilon_2^{(k)}(t)\right\}\big|\psi^{(k)}(t)\big\rangle, \tag{A2}$$

with the initial condition, $|\psi^{(k)}(t_{n-1})\rangle$. The envelope functions in Eqs. (A1) and (A2) are given by

$$\varepsilon_1^{(k)}(t) = \varepsilon_1^{(k-1)}(t) - \eta^{(k)}(t)\mathrm{Im}\big\langle\psi^{(k-1)}(t)|\xi^{(k)}(t)\big\rangle \times \big\langle\xi^{(k)}(t)\big|\alpha_B(r)\big|\psi^{(k-1)}(t)\big\rangle\varepsilon_2^{(k-1)}(t) \tag{A3}$$

and

$$\varepsilon_2^{(k)}(t) = \varepsilon_2^{(k-1)}(t) - \varsigma^{(k)}(t)\mathrm{Im}\big\langle\psi^{(k)}(t)\big|\xi^{(k)}(t)\big\rangle\big\langle\xi^{(k)}(t)\big|\alpha_B(r) \times \big|\psi^{(k)}(t)\big\rangle\varepsilon_1^{(k)}(t), \tag{A4}$$

where the step-dependent positive functions $\eta^{(k)}(t)$ and $\varsigma^{(k)}(t)$ determine the convergence behavior. Here, we assume $\eta^{(k)}(t) = \eta_0^{(k)}y(t)$ and $\varsigma^{(k)}(t) = \varsigma_0^{(k)}y(t)$. The function $y(t)$, defined by

$$y(t) = \begin{cases} \sin\left(\frac{t}{2\tau}\pi\right) & 0 \leqslant t < \tau \\ 1 & \tau \leqslant t \leqslant t_{\mathrm{f}} - \tau \\ \sin\left(\frac{t_{\mathrm{f}}-t}{2\tau}\pi\right) & t_{\mathrm{f}} - \tau < t \leqslant t_{\mathrm{f}} \end{cases}, \tag{A5}$$

with $\tau = 100$ fs, is introduced to avoid the rapid rise and decay of the optimal envelope function at both ends of the control period, t_0 and t_{f}. We thus adjust the two parameters, $\eta_0^{(k)}$ and $\varsigma_0^{(k)}$, during the iteration. As the function $y(t)$ has a flat structure, we also use it as an initial guess envelope to avoid introducing any bias in the iteration.

In our simulation, we found that the fixed intermediate control time t_n associated with $\bar{J}_n$ often imposes too strong constraints to realize high degrees of control achievement. Because of this, in every iteration step, we search the maximal value in the range of ±40 fs around the time t_n associated with the maximal value in the previous iteration step, and redefine the new final time t_n. In this way, we relax the restrictions due to the fixed control times when dealing with the intermediate targets.

Another numerical difficulty arises from $\varepsilon_2^{(k-1)}(t)$ and $\varepsilon_1^{(k)}(t)$ on the right-hand sides of Eqs. (A3) and (A4), respectively. When the iteration proceeds and the temporal peaks of the envelope grow larger, the increase in the peak amplitude will be fed back, resulting in the rapid increase in the peak amplitude, which often makes the iterative solution numerically unstable. To avoid this unfavorable feature, we usually need to adjust the magnitude of the step-dependent functions $\eta^{(k)}(t)$ and $\varsigma^{(k)}(t)$ in Eqs. (A3) and (A4).

In the present simulation, we adopt the following alternate method. According to the degrees of overall convergence, we divide the iteration steps into several "partially converged" stages, which are specified by "threshold" values of the peak amplitudes of the envelope. As an example, we consider the case in which we assume the threshold value $P^{(1)}$ in the first stage. If the value of $\varepsilon_1^{(k)}(t)$ $[\varepsilon_2^{(k)}(t)]$ exceeds $P^{(1)}$ at some time t, then $\varepsilon_1^{(k)}(t)$ $[\varepsilon_2^{(k)}(t)]$ is replaced with the threshold value such that $\varepsilon_1^{(k)}(t) = P^{(1)}$ $[\varepsilon_2^{(k)}(t) = P^{(1)}]$. Note that this modification keeps the monotonic convergence behavior of the iteration algorithm. We iteratively solve the coupled pulse-design equations to obtain the "partially converged" envelope, which would be composed of several rectangularlike envelopes. We then replace each rectangularlike envelope with a Gaussian envelope that has the same temporal width and pulse fluence as the corresponding envelope. Using these "partially converged" Gaussian envelopes, we restart the iteration by assuming the next threshold value. In the present simulation, we introduce three to eight partially converged stages to achieve the overall convergence, depending on the difficulty of the control problem.

APPENDIX B: ANALYTICAL APPROACH FOR EXAMINING CONTROL MECHANISMS IN FIG. 4

Because we do not see significant population transitions within the short control period [Fig. 4(c)], we can expand $|\psi(t)\rangle$ in the power series of $U(t) = -V_\alpha(r)[f(t)]^2/4$ such that $|\psi(t)\rangle = |\psi_0(t)\rangle + |\psi_1(t)\rangle + \cdots$. We then have

$$W(t) = |\langle\chi \mid \psi(t)\rangle|^2 = W_0(t) + W_1(t) + W_2(t) + \cdots, \tag{B1}$$

where

$$W_0(t) = |\langle\chi|e^{-iH_B^0 t/\hbar}|\chi\rangle|^2, \tag{B2}$$

$$\begin{aligned} W_1(t) &= 2\mathrm{Re}\langle\psi_0(t)|\chi\rangle\langle\chi|\psi_1(t)\rangle \\ &= \frac{2}{\hbar}\mathrm{Im}\langle\chi|e^{iH_B^0 t/\hbar}|\chi\rangle \int_0^t dt'\langle\chi|e^{-iH_B^0 t/\hbar}U_I(t')|\chi\rangle, \end{aligned} \tag{B3}$$

with $U_I(t') = e^{iH_B^0 t'/\hbar}U(t')e^{-iH_B^0 t'/\hbar}$. For convenience, we divide H_B^0 into the harmonic oscillator part and the anharmonic potential such that $H_B^0 = H_{\rm ho} + \delta V$. If the potential is harmonic, i.e., $\delta V = 0$, the wave packet returns its original shape at every vibrational period $T_{\rm ho}$, leading to $W_0(T_{\rm ho}) = 1$ and $W_1(T_{\rm ho}) = 0$. On the other hand, $W_1(T_{\rm ho}) \neq 0$ when $\delta V \neq 0$, which means that $W_1(T_{\rm ho})$ is the lowest-order, NIR-induced term that is directly connected to the anharmonicity. We thus examine $W_1(T_{\rm ho})$ to understand the dephasing suppression mechanisms. Because the effects of the population transitions and the anharmonicity are not so large within the short control period, we further approximate $e^{\pm iH_B^0 t/\hbar}$ in $|\psi_0(t)\rangle$ and $|\psi_1(t)\rangle$ up to first order and zeroth order with respect to δV, respectively. Then, Eq. (B3) at $t = T_{\rm ho}$ is approximated by

$$\begin{aligned} W_1(T_{\rm ho}) \simeq \frac{2}{\hbar}\int_0^{T_{\rm ho}} dt''\langle\chi|\delta V_I(t'')|\chi\rangle \\ \times \int_0^{T_{\rm ho}} dt'\langle\chi|U_I(t')|\chi\rangle > 0, \end{aligned} \tag{B4}$$

with $\delta V_I(t'') = e^{iH_{\rm ho}t''/\hbar}\delta V e^{-iH_{\rm ho}t''/\hbar}$. The positive value of Eq. (B4) comes from the fact that the operators δV and $U(t)$ are nonpositive in the present study. As the interference term

TABLE I. Results of $|\langle\chi|\psi(t_{\rm f})\rangle|^2$ from $t_{\rm f} = 2835$ fs to $t_{\rm f} = 2855$ fs at every 5 fs.

$t_{\rm f}$	2835 fs	2840 fs	2845 fs	2850 fs	2855 fs
$\vert\langle\chi\vert\psi(t_{\rm f})\rangle\vert^2$	0.9994	0.9995	0.9996	0.9997	0.9998

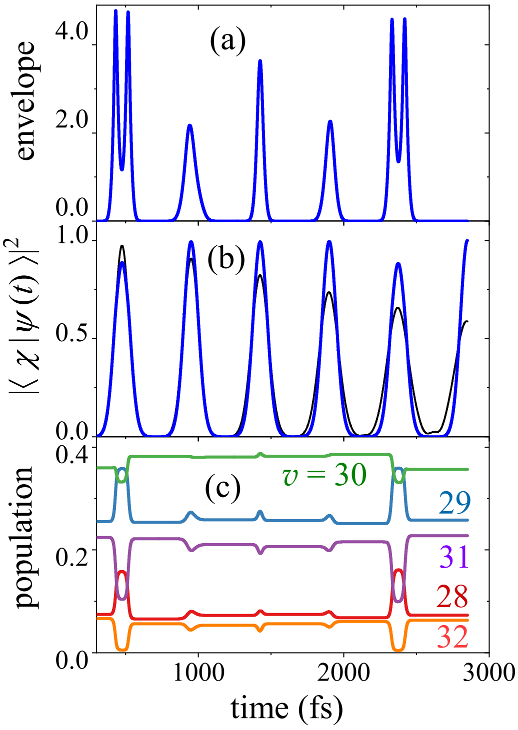

FIG. 11. Results of optimal control simulation when a single target ($N = 1$) and a fixed control time $t_{\rm f} = 2850$ fs are assumed. The temporal width of the pump pulse is set to 80 fs. The convergence criterion in this example is that the target value is greater than 0.999. (a) Optimal envelope function $f(t)$, (b) $|\langle\chi|\psi(t)\rangle|^2$ with (blue line) and without (black line) the optimal pulse, and (c) time evolution of populations of five major vibrational eigenstates in $|\psi(t)\rangle$.

$W_1(T_{\text{ho}})$ always contributes to the increase of the value of $W(T_{\text{ho}})$, we conclude that the primary mechanism of the dephasing suppression induced by the NIR pulse is attributed to $W_1(t)$, i.e., the interference between the original wave packet and the NIR-induced component. A pulse train with a nearly regular time interval, T_{ho}, effectively suppresses the dephasing at least within a short temporal period.

APPENDIX C: RIGOROUS CONTROL WITH SHORT CONTROL TIME

If we consider the applications to quantum information, the error due to the dephasing should be on the order of 10^{-4}. Motivated by this, we try to realize such an extremely precise control *regardless* of experimental feasibility. Here, we design optimal pulses with the aim of achieving $|\langle\chi|\psi(t_{\text{f}})\rangle|^2 \geqslant 0.999$ when adopting the pump pulse with 80 fs FWHM and assuming a single target around $t_{\text{f}} = 2850$ fs. Table I summarizes the results of $|\langle\chi|\psi(t_{\text{f}})\rangle|^2$ from $t_{\text{f}} = 2835$ fs to $t_{\text{f}} = 2855$ fs at every 5 fs. A longer control period tends to achieve a slightly larger value of $|\langle\chi|\psi(t_{\text{f}})\rangle|^2$ within the temporal range considered here. As we find that the designed optimal pulses have almost the same structures, we show one of the results in Fig. 11 as a typical example. Contrary to the optimal pulse in Fig. 4(a), the optimal pulse in Fig. 11(a) has a temporally symmetric but highly structured shape. The first and final pulse components have double-peak structures and induce large "round-trip" population transitions, whereas the other pulse components induce quite small population transitions. If we scrutinize the population of the $|v_B = 30\rangle$ state, i.e., the largest component of $|\psi(t)\rangle$, it is almost constant during the control period. On the other hand, the populations of the $|v_B = 31\rangle$ and $|v_B = 32\rangle$ states (the $|v_B = 28\rangle$ and $|v_B = 29\rangle$ states) are first deexcited (excited) and then excited (deexcited) at a short time interval. During the periods, the relative phases associated with those vibrational states evolve faster (slower) in time because of the larger (smaller) energy difference. The population transitions apparently adjust the relative phases between the adjacent vibrational states. As shown, for example, in Fig. 4, the control pulse that only induces small population transitions can suppress the dephasing with high probability. On the other hand, to suppress the dephasing with extremely high precision, the control pulse further adjusts the relative phases in the wave packet by utilizing "round-trip" population transitions.

[1] H.-P. Breuer and F. Petruccione, *The Theory of Open Quantum Systems* (Oxford University Press, New York, 2002).

[2] M. Schlosshauer, *Decoherence and the Quantum-to-Classical Transition* (Springer-Verlag, Berlin, 2007).

[3] J. A. Yeazell and C. R. Stroud, Jr., Phys. Rev. Lett. **60**, 1494 (1988).

[4] A. Buchleitner, D. Delande, and J. Zakrzewski, Phys. Rep. **368**, 409 (2002).

[5] H. Maeda, D. V. L. Norum, and T. F. Gallagher, Science **307**, 1757 (2005).

[6] A. Amo, S. Pigeon, D. Sanvitto, V. G. Sala, R. Hivet, I. Carusotto, F. Pisanello, G. Lemenager, R. Houdre, E. Giacobino, C. Ciuti, and A. Bramati, Science **332**, 1167 (2011).

[7] T. Yefsah, A. T. Sommer, M. J. H. Ku, L. W. Cheuk, W. Ji, W. S. Bakr, and M. W. Zwierlein, Nature (London, UK) **499**, 426 (2013).

[8] O. A. Egorov, D. V. Skryabin, A. V. Yulin, and F. Lederer, Phys. Rev. Lett. **102**, 153904 (2009).

[9] H. Katsuki, Y. Ohtsuki, T. Ajiki, H. Goto, and K. Ohmori, arXiv:1910.08241 [Phys. Rev. Research (to be published)].

[10] B. Sussman, D. Townsend, M. Yu. Ivanov, and A. Stolow, Science **314**, 278 (2006).

[11] P. J. Bustard, R. Lausten, D. G. England, and B. J. Sussman, Phys. Rev. Lett. **111**, 083901 (2013).

[12] K. Ohmori, Ann. Rev. Phys. Chem. **60**, 487 (2009).

[13] A. González-Castrillo, F. Martín, and A. Palacios, Sci. Rep. **10**, 12981 (2020).

[14] D. Azoury, O. Kneller, S. Rozen, B. D. Bruner, A. Clergerie, Y. Mairesse, B. Fabre, B. Pons, N. Dudovich, and M. Krüger, Nat. Photonics **13**, 54 (2019).

[15] Y. Ohtsuki, H. Goto, H. Katsuki, and K. Ohmori, Phys. Chem. Chem. Phys. **16**, 5689 (2014).

[16] Y. Ohtsuki and K. Nakagami, Phys. Rev. A **77**, 033414 (2008).

[17] K. Nakagami, Y. Mizumoto, and Y. Ohtsuki, J. Chem. Phys. **129**, 194103 (2008).

[18] D. J. Tannor, *Introduction to Quantum Mechanics: A Time-Dependent Perspective* (University Science Books, Sausalito, CA, 2007), Chap. 16.

[19] C. Brif, R. Chakrabarti, and H. Rabitz, New J. Phys. **12**, 075008 (2010).

[20] S. J. Glaser *et al.*, Eur. Phys. J. D **69**, 279 (2015).

[21] H. Rabitz, R. de Vivie-Riedle, M. Motzkus, and K. Kompa, Science **288**, 824 (2000).

[22] T. Nöbauer, A. Angerer, B. Bartels, M. Trupke, S. Rotter, J. Schmiedmayer, F. Mintert, and J. Majer, Phys. Rev. Lett. **115**, 190801 (2015).

[23] P. Rembold, N. Oshnik, M. M. Müller, S. Montangero, T. Calarco, and E. Neu, AVS Quantum Sci. **2**, 024701 (2020).

[24] J. C. Saywell, I. Kuprov, D. Goodwin, M. Carey, and T. Freegarde, Phys. Rev. A **98**, 023625 (2018).

[25] R. Heck *et al.*, Proc. Natl. Acad. Sci. USA **115**, E11231 (2018).

[26] W. Zhu, J. Botina, and H. Rabitz, J. Chem. Phys. **108**, 1953 (1998).

[27] Y. Ohtsuki, W. Zhu, and H. Rabitz, J. Chem. Phys. **110**, 9825 (1999).

[28] Y. Ohtsuki, K. Nakagami, Y. Fujimura, W. Zhu, and H. Rabitz, J. Chem. Phys. **114**, 8867 (2001).

[29] J. Somlói, V. A. Kazakov, and D. J. Tannor, Chem. Phys. **172**, 85 (1993).

[30] A. Bartana, R. Kosloff, and D. J. Tannor, J. Chem. Phys. **106**, 1435 (1997).

[31] N. Khaneja, T. Reiss, C. Kehlet, T. Schulte-Herbrüggen, and S. J. Glaser, J. Magn. Reson. **172**, 296 (2005).

[32] P. de Fouquieres, S. G. Schirmer, S. J. Glaser, and I. Kuprov, J. Magn. Reson. **212**, 412 (2011).

[33] H-J. Hogben, M. Krzystyniak, G. T. P. Charnock, P. J. Hore, and I. Kuprov, J. Magn. Reson. **208**, 179 (2011).

[34] W. Kallies and S. J. Glaser, J. Magn. Reson. **286**, 115 (2018).

[35] F. Martin, R. Bacis, S. Churassy, and J. Vegès, J. Mol. Spectrosc. **116**, 71 (1986).

[36] R. F. Barrow and K. K. Yee, J. Chem. Soc., Faraday Trans. 2 **69**, 684 (1973).

[37] H. Goto, H. Katsuki, H. Ibrahim, H. Chiba, and K. Ohmori, Nat. Phys. **7**, 383 (2011).

[38] K. Blum, *Density Matrix Theory and Applications* (Plenum Press, New York, 1981).

[39] M. Lapert, R. Tehini, G. Turinici, and D. Sugny, Phys. Rev. A **78**, 023408 (2008).

[40] D. M. Reich, M. Ndong, and C. P. Koch, J. Chem. Phys. **136**, 104103 (2012).

[41] M. Ndong, M. Lapert, C. P. Koch, and D. Sugny, Phys. Rev. A **87**, 043416 (2013).

[42] Y. Ohtsuki and W. Domcke, in *Conical Intersections: Theory, Computation and Experiment*, edited by W. Domke, D. R. Yarkony, and H. Köppel (World Scientific, Singapore, 2011), Chap. 14.

[43] P. Luc, J. Mol. Spectrosc. **80**, 41 (1980).

[44] J. Tellinghisen, J. Chem. Phys. **134**, 084301 (2011).

[45] G. Maroulis, C. Makris, U. Hohm, and D. Goebel, J. Phys. Chem. A **101**, 953 (1997).

[46] P. R. Berman and V. S. Malinovsky, *Principles of Laser Spectroscopy and Quantum Optics* (Princeton University Press, Princeton, NJ, 2011).